

Relationship between hardness and dislocation processes in a nanocrystalline metal at the atomic scale

Frederic Sansoz*

School of Engineering and Materials Science Program, The University of Vermont, Burlington, VT 05405, USA

Kevin D. Stevenson

School of Engineering, The University of Vermont, Burlington, VT 05405, USA

(Received 18 February 2011; revised manuscript received 25 March 2011; published 9 June 2011)

By combining atomic force microscopy (AFM) and large-scale molecular dynamics (MD) simulations, we examine at comparable scales the atomistic processes governing nanohardness in electrodeposited nanocrystalline Ni with a mean grain diameter of 18.6 nm under confined contact deformation. Notably, this mean grain diameter represents the “strongest” size for Ni and other nanocrystalline materials where both crystal slip and grain-boundary deformation processes are intertwined to accommodate plastic flow. Accurate hardness measurements were obtained from shallow nanoindentations, less than 10 nm in depth, using an AFM diamond tip. We show evidence that the controlling yielding mechanism in the peak of hardness as a function of penetration depth corresponds to the emission of partial dislocations from grain boundaries. However, MD simulations also reveal for this grain size that the crystalline interfaces must undergo significant sliding at small penetration depths in order to initiate crystal slip. The strong interplay between intergranular and intragranular deformation processes found in this model nanocrystalline metal is discussed and shown to considerably reduce the local dependence of nanohardness on the initial microstructure at this scale, unlike past observations of nanoindentation in Ni electrodeposits with larger grain sizes. These new findings therefore constitute an important step forward to understanding the contribution of nanoscale grain-boundary networks on permanent deformation and hardness relevant for nanoscale materials and structures.

DOI: [10.1103/PhysRevB.83.224101](https://doi.org/10.1103/PhysRevB.83.224101)

PACS number(s): 62.25.-g, 62.20.Qp, 61.72.Ff, 61.72.Mm

I. INTRODUCTION

Mechanical strength in polycrystalline materials like metals is known to increase monotonically with the inverse square root of grain size due to the classical Hall–Petch effect.^{1,2} Nanocrystalline materials with grains less than 50 nm in diameter, however, possess a distinctive mechanical behavior compared with coarse-grained polycrystals. Remarkably, this type of material exhibits a peak in elastic limit and hardness under deformation at a critical grain size, defining the so-called “strongest” size.^{3,4} This phenomenon has been understood for some time in bulk nanostructures in terms of the dominant mode of plastic deformation at the atomic scale. Both model experiments and atomistic computer simulations have proved that a fundamental shift from grain-boundary-assisted crystal slip to grain-boundary-localized deformation, such as grain-boundary sliding and migration, takes place during grain refinement in nanocrystalline materials.^{5–30} Understanding the influence of nanoscale grain-boundary networks on nanohardness in atomic-scale contacts is therefore increasingly important for synthesizing thin films and nanoscale devices with improved resistance to contact deformation and failure.

Past models of plastic yielding during the nanoindentation of polycrystals are based on the nucleation and propagation of dislocations and their interaction with surrounding grain boundaries beneath penetrating tips. A typical sequence of plastic flow consists of the homogeneous nucleation of dislocations under the contact zone and their glide through the indented crystal.^{31,33} This process is followed by either slip arrest or dislocation absorption by neighboring interfaces.^{34–37} By performing nanoindents in the center of individual grains

smaller than 850 nm in Ni electrodeposits, Yang and Vehoff³⁷ have observed that the permanent displacement jump caused by the nucleation of new dislocations decreased, and the nanohardness increased, with decreasing grain size. Because the grains were large compared to the contact size, they argued that new dislocations interacted directly with only adjacent grain boundaries. For nanoscale contacts, however, such processes become highly complex and stochastic, and therefore more difficult to verify experimentally, because the distance between indentation site and the closest interface is mostly random and the mean contact pressure at yield point depends on both the crystal orientation and the local grain boundary structure.^{38,39} Also, the above model breaks down when the contact zone becomes larger than the mean grain diameter, particularly in the nanoindentation of nanocrystalline materials with grains less than 20 nm in diameter.⁴⁰ As a result, cooperative deformation processes involving grain boundaries such as dislocation emission,^{13,36,41} twinning,^{42,43} grain rotation, and stress-assisted grain coarsening^{23,26,29,44–46} can simultaneously act to accommodate plastic flow during nanoindentation. However, among all deformation processes at play, the fundamental mechanism that predominantly controls materials hardness at this scale is not fully understood. Furthermore, the relationship between experimental nanohardness and underlying molecular processes remained largely unexplored in this type of material.

In this paper, using a combined experimental and computational approach at the atomic scale, we report on accurate nanohardness measurements and microstructure evolution in electrodeposited nanocrystalline Ni under confined contact deformation with an atomic force microscopy (AFM) diamond tip. A salient feature of the present investigation is the

combination of AFM nanoindentation experiments and large-scale molecular dynamics (MD) simulations, which made it possible, to our knowledge, for the first time to attain comparable scales of analysis in terms of grain size and contact zone-size during spherical nanoindentation. Also, the electrochemical environment during material synthesis has been optimized in order to produce a fully dense Ni microstructure with a critical grain size at the maximum of hardness. In the following sections, we show clear evidence that a peak of hardness as a function of penetration depth is observed, and we elucidate the dislocation processes controlling this phenomenon for very shallow indentations less than 10 nm in depth. Furthermore we demonstrate that the nanohardness of nanocrystalline Ni electrodeposits at depths larger than 2.5 nm is not significantly affected by local differences in microstructure despite the stochastic nature of confined deformation in nanoscale grain-boundary networks.

II. METHODS

A. Material synthesis

Direct-current (dc) electrodeposition of pure Ni was performed on a polished Si (100) wafer at 50 °C under constant current density (18 mA cm⁻²) until the deposit was about 40 μm in thickness.⁴⁷ The anode material was a 99.9945%-purity Ni foil. The bath consisted of Ni sulfamate (400 g L⁻¹) with a small amount of Ni chloride (10 g L⁻¹) and boric acid (30 g L⁻¹). 2.0 g L⁻¹ of Ni carbonate were used to raise the pH value by increments of 0.2. The Ni carbonate was mechanically agitated in the bath for 30 min. At the desired pH, the entire solution was vacuum filtered through a 1.3-μm paper filter to remove any Ni carbonate precipitates. Conversely, amidosulfamic acid was used to lower the pH if necessary. The pH investigated in this study was equal to 4.5. We added 2 mL L⁻¹ of dipolar surfactant (NP-M2 antipitting agent) to decrease the surface tension of the solution and release hydrogen gas from the substrate. 0.2 g L⁻¹ of 2-butyne-1,4-diol and 1.0 g L⁻¹ of saccharin were added to promote both grain refinement and ultralow surface roughness. We adjusted the pH value when saccharin was added to the bath, while maintaining the solution temperature at 50 °C to prevent saccharin from precipitating out. The plating bath was stirred at a constant rate. The sample was thoroughly rinsed in distilled water after plating, and cleaned in ethanol. Contact-mode AFM imaging was performed in air using standard Si cantilevers (Mikromasch CSC17; tip radius <10 nm; force constant ~0.15 N/m) to determine the root-mean-square (rms) surface roughness of the electrodeposited specimen. The scan rate was 1 Hz with a resolution of 400 lines per scan. Three 1 × 1 μm² AFM scans were repeated at different locations on the surface to obtain an average value of rms roughness.

B. AFM nanoindentation

AFM nanoindentation experiments were carried out using a universal scanning probe microscope (Quesant, Santa Cruz, CA) with a closed-loop metrology scanner consisting of XYZ capacitive displacement sensors. Following the manufacturer's calibration procedure, positioning precisions of 6.5, 9.6, and 0.1 nm were measured along the X, Y, and Z directions, respectively, for a maximum XY scan size of 40 × 40 μm² and a

vertical Z range of 6.11 μm. A sapphire AFM cantilever with a specifically designed cube-corner, single-crystal diamond tip (both the cantilever and the tip were assembled by Micro Star Technologies, Huntsville, TX) was used to perform the AFM imaging and nanoindentation on the electrodeposited Ni specimen. A finite element analysis was used to determine the normal spring constant of this cantilever,⁴⁸ which was found equal to 906 N m⁻¹. The area function of the tip and the radius of curvature at the tip apex were obtained by scanning the probe over a TGT1 Si grating made of 750-nm-high inverted Si tips, and by analyzing the resulting image with the tip detection feature in the software Scanning Probe Image Processor (Image Metrology, Denmark). Calibration to obtain quantitative nanohardness measurements from AFM nanoindentation was performed with a fused quartz specimen following the force-matching method described elsewhere.⁴⁸ The indentation hardness H was estimated from

$$H = \frac{F_{\max}}{A_c}, \quad (1)$$

where F_{\max} is the peak load applied by the diamond tip and A_c is the corresponding projected area of contact based on the area of the residual impression after unloading. To determine A_c accurately, we first measured *in situ* the residual depth h_c of the permanent indentation after unloading by noncontact topographical AFM imaging with the diamond tip. Second, h_c was substituted into the tip area function established above. Here it was assumed that the difference between contact depth and residual depth is negligible for shallow indentations in Ni.

C. MD simulations

MD simulations were conducted using Large-scale Atomic/Molecular Massively Parallel Simulator⁴⁹ with an embedded-atom method interatomic potential for Ni from Mishin *et al.*⁵⁰ Two films consisting of 24 grains with a mean size of 18.6 nm were modeled with different distributions of grains and crystallographic orientations following a previous computational methodology.⁵¹ The film dimensions were 70 nm × 70 nm × 35 nm, which used ~16 million atoms. Periodic boundary conditions were applied to the film sides except for the loading direction. Prior to deformation, the models were relaxed using an energy minimization with a conjugate gradient method, followed by a zero-stress relaxation in the isothermal-isobaric ensemble (constant number of particles, pressure, and temperature, NPT) using a Nosé-Hoover thermostat at 300 K for 100 ps (20,000 steps). The time step was 5 fs. After relaxation, the bottom two atomic layers were fixed in all directions and deformation was performed at 300 K in the canonical ensemble (constant number of particles, volume and temperature, NVT). As in a past atomistic study, Ref. 52 a virtual tip was modeled by a spherical, repulsive force of magnitude

$$F(r) = -k(r - R)^2, \quad (2)$$

where r is the distance from an atom to the center of the tip, R is the tip radius (=50 nm), and k is a force constant (=10 N/m²). A gap of 0.5 nm was initially imposed between the sample surface and the tip. In this study, the tip was displaced at a rate of 1 m s⁻¹ into the film surface. The final penetration depth was

4.25 nm. The contact zone was defined by the atoms positioned within the boundary of the tip (i.e., $r < R$). As such, the mean contact pressure p_m was calculated as

$$p_m = \frac{P}{A}, \quad (3)$$

where P is the total load applied by the tip to the contacted atoms, and A is the projected contact area, which was directly measured from the position of the contacted atoms. In our atomistic simulations, it was found that the shape of the contact area was irregular, due to the discrete number of atoms; but for simplicity, the contact area was approximated by an elliptical shape. Furthermore, the mechanisms of plastic deformation were studied using the local crystal structure analysis⁵³ and the least-square atomic local shear strain invariant calculations⁵⁴ in the atomistic configuration viewer AtomEye.⁵⁵ Here, atoms in dark color correspond to atoms undergoing negligible plastic deformation, while atoms in severely deformed zones with more than 30% deformation appear in white color. The simulations presented in this paper required ~180,000 computer processing unit (CPU) hours (~20.5 CPU year) on an x3455 IBM high-performance computing system.

III. RESULTS

A. Material structure and microhardness

After synthesis, the Ni electrodeposit exhibited a uniform nanocrystalline microstructure and an ultrasmooth surface morphology. As discussed in earlier studies,^{56–58} both current density and pH of the solution were adjusted to optimize

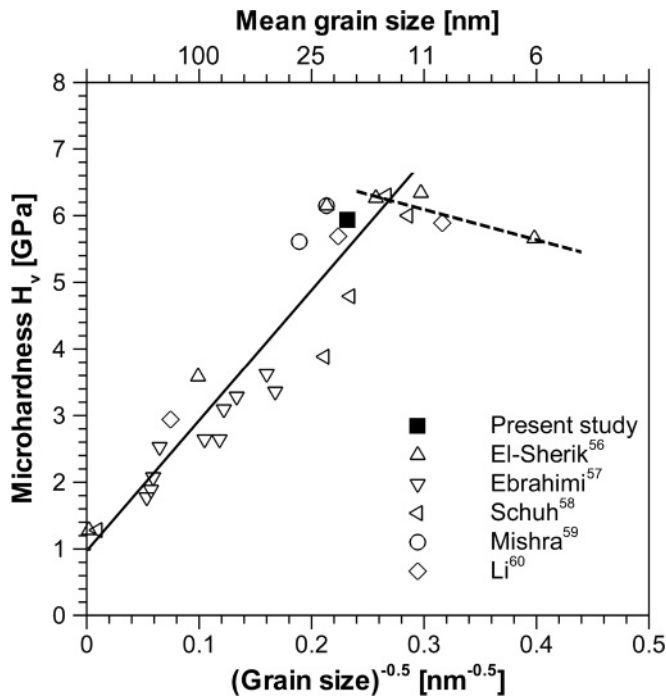


FIG. 1. Representation of microhardness in pure electrodeposited nanocrystalline Ni from the present study and the literature.^{56–60} The “strongest” size can be found at the crossover in microhardness from classical Hall–Petch regime (solid line) to inverse regime (dashed line). We note that only data with low saccharin content have been used for the results of Mishra and Balasubramaniam.⁵⁹

the grain-size distribution during electrodeposition. The mean grain size was found equal to 18.6 nm as determined by (111) and (200) x-ray diffraction peak broadening. The rms surface roughness of the film was found equal to $2.32 \text{ nm} \pm 0.3 \text{ nm}$, which is significantly smaller than that in electroplated Ni films with coarse grain sizes.⁴⁷ We could not find any trace of oxide from both light optical and scanning electron microscopy inspections. The microhardness of the nanocrystalline Ni electrodeposit was found equal to $5.93 \pm 0.13 \text{ GPa}$ at an applied load of ~500 mN. For comparison, this property is represented in a Hall–Petch plot in Fig. 1 along with past results from the literature^{56–60} for pure electrodeposited Ni. This figure shows that the crossover in microhardness from the classical Hall–Petch regime to the inverse regime occurs at a mean grain size of $16.1 \pm 4.7 \text{ nm}$. This value therefore suggests that the characteristics of our specimen were close to those in nanocrystalline Ni electrodeposits with the “strongest” size.

B. Nanoindentation behavior

Figure 2(a) presents a topographical AFM image of nine nanoindentations performed with a cube-corner diamond tip

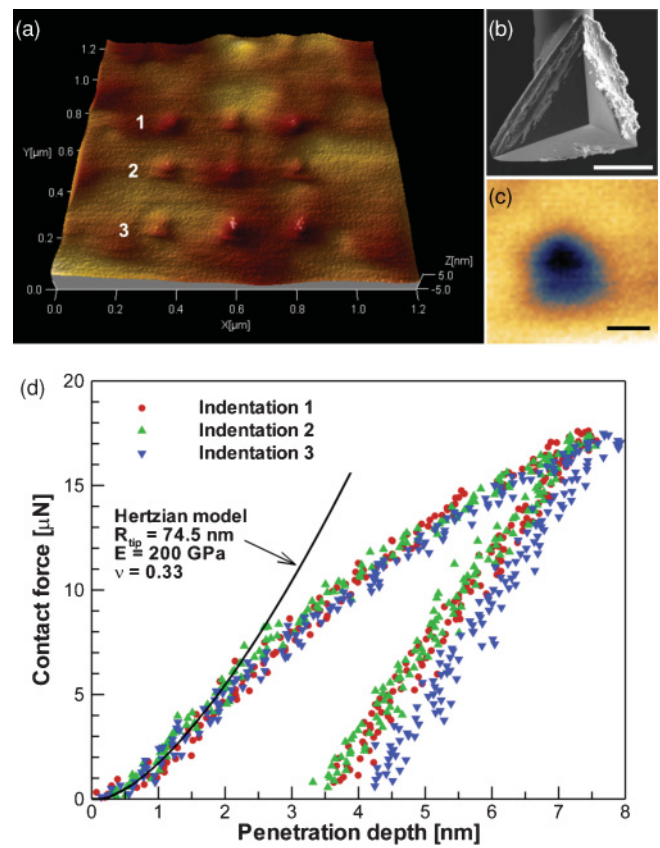


FIG. 2. (Color online) AFM nanoindentations in a 40- μm -thick Ni film with a mean grain diameter of 18.6 nm electrodeposited on a polished Si wafer. (a) $1.2 \mu\text{m} \times 1.2 \mu\text{m}$ noncontact topographical AFM image of nine nanoindentations conducted with a peak load of $18 \mu\text{N}$. (b) Close-up view on cube-corner diamond tip mounted on an AFM sapphire cantilever. Scale bar, $50 \mu\text{m}$. (c) Top topographical AFM view of indent 1. Scale bar, 20 nm . (d) Force–penetration depth curves corresponding to indents 1–3. The line represents the prediction from Hertzian elastic contact theory.

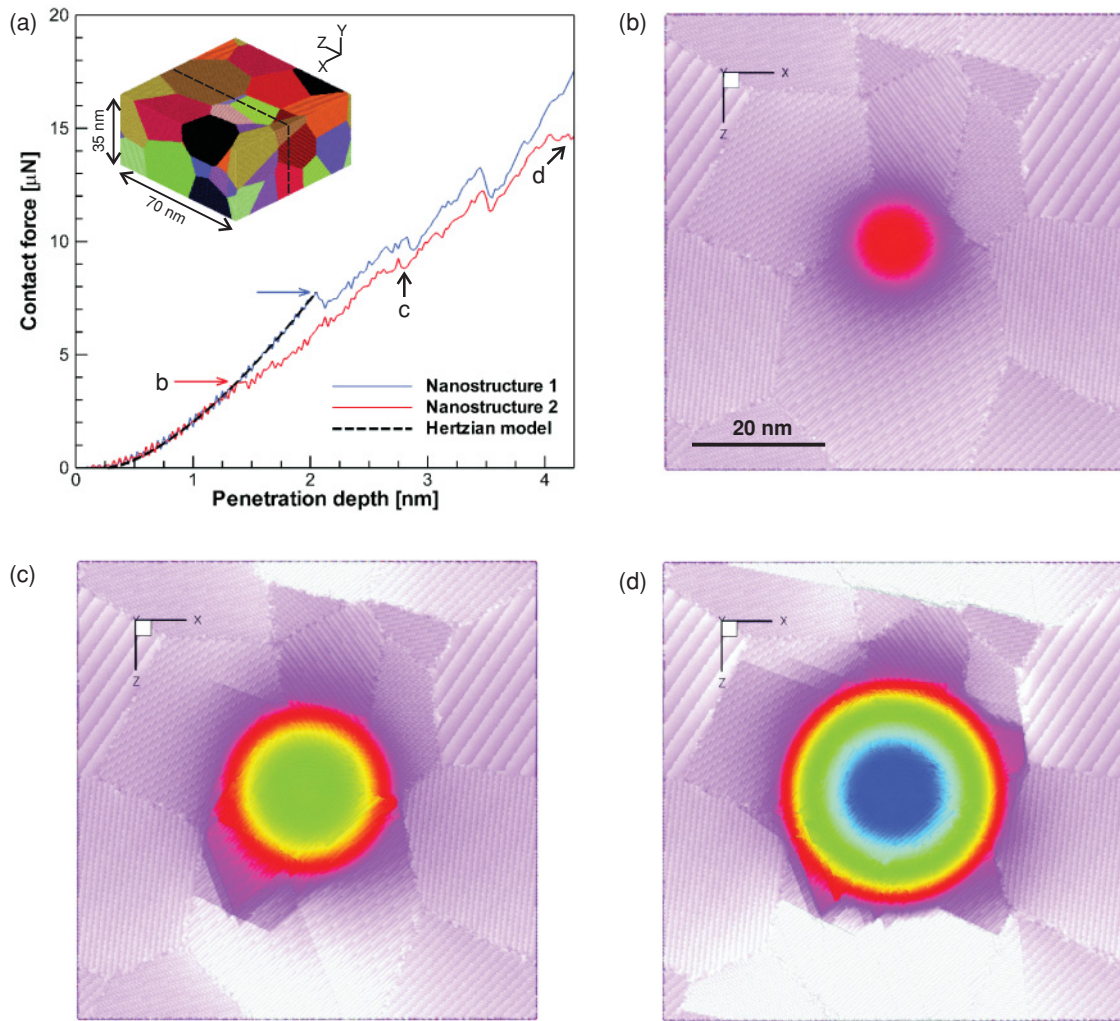


FIG. 3. (Color online) Large-scale three-dimensional MD simulations of spherical indentation in 35-nm-thick Ni films with a mean grain size of 18.6 nm. The contacting tip is 50 nm in radius. (a) Nanoindentation force–penetration depth curves for two films simulated with different initial microstructures. The dashed line represents the prediction from Hertz elastic contact theory. The inset represents the three-dimensional grain morphology of nanostructure 2. (b), (c), (d) Atomic-level snapshots of the top surface of nanostructure 2 during indentation. The coloring corresponds to the atomic position in the direction normal to the surface. Surface atoms with high and low positions appear in white and blue colors, respectively.

[Fig. 2(b)] mounted on an AFM sapphire cantilever.⁴⁸ Each test in this figure was carried out under the same peak load of 18 μN, thereby resulting in penetration depths of 8 nm or less. For such small penetration depths, the contact deformation can be considered as semispherical because the curvature at the tip apex was found equal to 74.5 nm in radius and the residual impressions left on the surface after unloading were quasi-circular [Fig. 2(c)]. Figure 2(d) shows the force—penetration depth curves corresponding to indents 1–3 as indicated in Fig. 2(a). No marked differences could be detected between the different loading curves at identical penetration depths. This result proves experimentally that the nanoindentation behavior does not significantly depend on local variations of microstructure. Furthermore, we compared the nanoindentation response of our specimen with the prediction from Hertz elastic contact theory⁶¹ using the elastic properties for pure Ni (Young’s modulus and Poisson’s ratio equal to 200 GPa and 0.33, respectively). Figure 2(d) shows

that both elastic theory and experimental data are in excellent agreement up to a penetration depths of ~2 nm, which tends to indicate that the nanocrystalline specimen investigated behaved purely elastically up to this depth. Also, contrary to prior nanoindentation studies in nanocrystalline materials with larger grain sizes and contact zones,³⁷ no displacement discontinuity was observed in the plastic portion of the loading curve. Therefore this observation allowed us to conclude that the onset of plastic flow during nanoindentation was controlled by a gradual process rather than by homogenous crystal slip.³¹

By way of comparison, Fig. 3 presents the nanoindentation behavior of the two 35-nm-thick nanocrystalline Ni films as obtained by large-scale MD simulations. The evolution of the contact force as a function of penetration depth represented in this figure revealed two major findings. First, the microstructure was found to strongly influence the yield point, which is characterized by a departure of the nanoindentation curve from the Hertzian elastic model. For example, Fig. 3(a) shows that

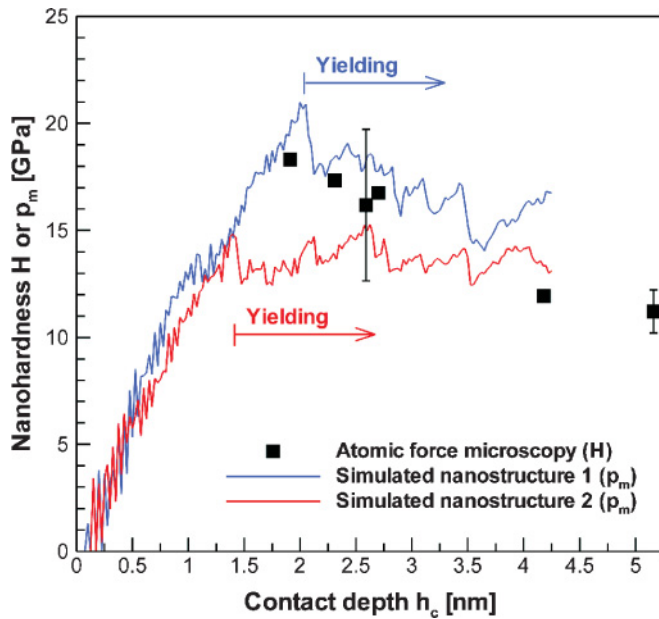


FIG. 4. (Color online) Comparison of nanohardness (H) obtained from AFM experiments with mean contact pressures (p_m) predicted by MD simulations as functions of contact depth h_c . The error bars for some experimental data represent the standard deviation obtained from 3×3 grids of nanoindentations performed at the same peak load.

the yielding load in nanostructure 1 ($7.8 \mu\text{N}$) is twice as large as that in nanostructure 2 ($3.8 \mu\text{N}$). We also note here that plastic deformation first occurred at a penetration depths of 2 nm and 1.42 nm in nanostructures 1 and 2, respectively, which is consistent with the experimental findings above. Second, it was found that the two nanoindentation curves converged to similar values at penetration depths larger than 2.5 nm. Therefore it appeared that the nanoindentation behavior became less microstructure dependent with increasing penetration depths. Furthermore our MD simulations showed that several grains were plastically deformed during contact loading. For instance, in Figs. 3(b), 3(c), and 3(d), it can be observed in simulated nanostructure 2 that the contact zone included at least three grains from the yield point (depth = 1.42 nm) to the maximum depth of penetration (depth = 4.25 nm). These figures also show significant planar slip inside the grains and some sliding between the crystals, as indicated by the color contrast in Fig. 3(d). This observation therefore provides strong evidence for the occurrence of both intragranular and intergranular deformation mechanisms during nanoindentation in this type of materials.

The evolution of mean contact pressure predicted for each simulated nanostructure is represented in Fig. 4 as a function of contact depth h_c . This figure shows that p_m increases during the elastic portion of the loading curve before reaching a yielding point at depths between 1.4 and 2.0 nm. The increase of mean contact pressure for penetration depths less than 2 nm in our MD simulations is similar to past atomistic predictions in Ni single-crystalline thin films deformed by spherical indentation.⁵² This effect is due to the method used to determine the contact area in simulation, which differs from that in experiments, and therefore should not be regarded as

physically meaningful until yielding occurs. Nevertheless, it can be observed in Fig. 4 that p_m varies, as a function of indented microstructure, more so near the yield point (between 14 and 22 GPa) than at larger contact depths.

Furthermore, p_m was compared in Fig. 4 with the nanohardness H obtained from AFM measurements, as a function of contact depth h_c . In particular, it has been shown in an earlier study⁴⁸ that h_c can be more easily related to the contact area at peak load in AFM experiments. Figure 4 includes experimental results from 20 nanoindentations at different peak loads (data presenting error bars have been obtained by repeating tests at the same load). No permanent indents smaller than 2 nm in depth were found experimentally, which supports the fact that the deformation is mostly elastic up to this contact depth as discussed above. Figure 4 shows that the film hardness increases as the contact depth decreases, which can be related to nanoindentation size effects observed in pure Ni,⁶² as discussed in more detail below. This figure also shows that computational predictions and experimental results are in excellent agreement. Also, it is important to note that the error in nanohardness measurements significantly increased with decreasing depth, which confirms that the yielding process was more sensitive to the underlying microstructure at small contact depths as predicted in MD simulations.

C. Deformation Mechanisms

An atomic-level analysis based on local crystal structure⁵³ and local shear-strain-invariant⁵⁴ calculations is shown in Figs. 5 and 6, respectively, for different steps of deformation in simulated nanostructure 2. For brevity, in the following, we discuss only the results obtained within a slice of 1 nm in thickness parallel to the YZ plane and located in the center of the film, as represented by the dashed line in the inset of Fig. 3(a). We can see in Fig. 5(b) that the onset of plasticity corresponding to the apparent yield point is due to the nucleation and propagation of a full $\{111\}\langle 110\rangle$ dislocation (highlighted by an arrow) from a grain boundary indented by the tip. With full atomistic details, the simulation shows the dissociation of this dislocation into two $\{111\}\langle 112\rangle$ partial dislocations connected by a stacking fault nanoribbon (atoms in yellow color), which is commonly observed in face-centered-cubic (fcc) metals like Ni. As further deformation proceeds, Figs. 5(c) and 5(d) reveal that more grain boundaries (highlighted by a vertical arrow) start to emit partial dislocations away from the contact zone. Subsequently, these dislocations formed either full dislocations or deformation twins. A key result shown in Fig. 6 is that significant shear strain in excess of 30% was found on several interfaces prior to the emission of the first partial dislocations, as well as later in the dislocation dynamic process. Such high shear strains are typically encountered in the localized sliding of crystalline interfaces via grain-boundary atom shuffling and free-volume migration.^{8,11,63} This result therefore points to an important conclusion on the interplay between two mechanisms: Significant grain-boundary sliding was required to initiate the emission of lattice dislocations from grain boundaries, which in turn was the controlling factor influencing nanohardness in our nanocrystalline Ni specimen.

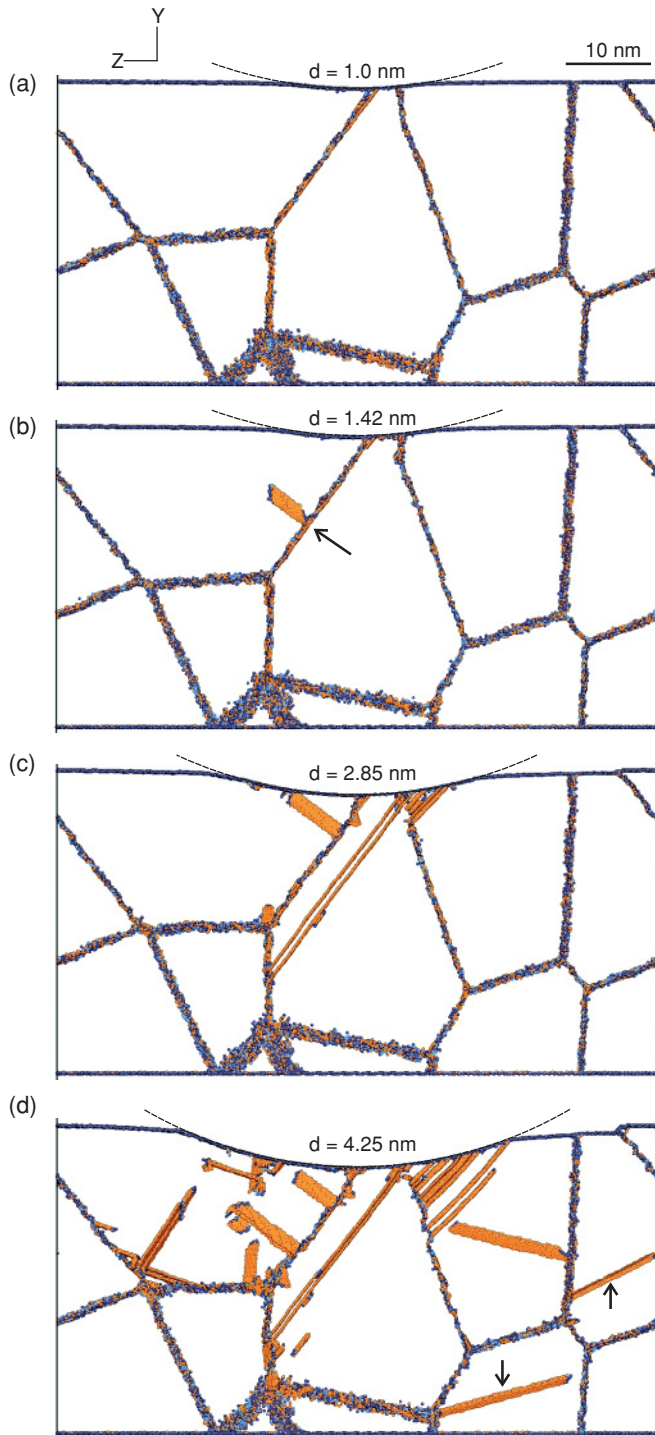


FIG. 5. (Color online) Atomistic processes of dislocation nucleation and propagation from grain boundaries in nanostructure 2 using local crystal structure analysis.⁵³ Atoms in fcc arrangements have been omitted for clarity. Those in hcp arrangements such as stacking fault planes are shown in yellow color while uncorrelated atoms such as grain boundary and surface atoms appear in blue color.

In what follows, we examine in detail the origin of the significant variation in nanohardness at yield point, as a function of microstructure, with particular emphasis on the primary mechanism controlling the onset of plasticity. For that purpose, a magnified view on the first yielding event in

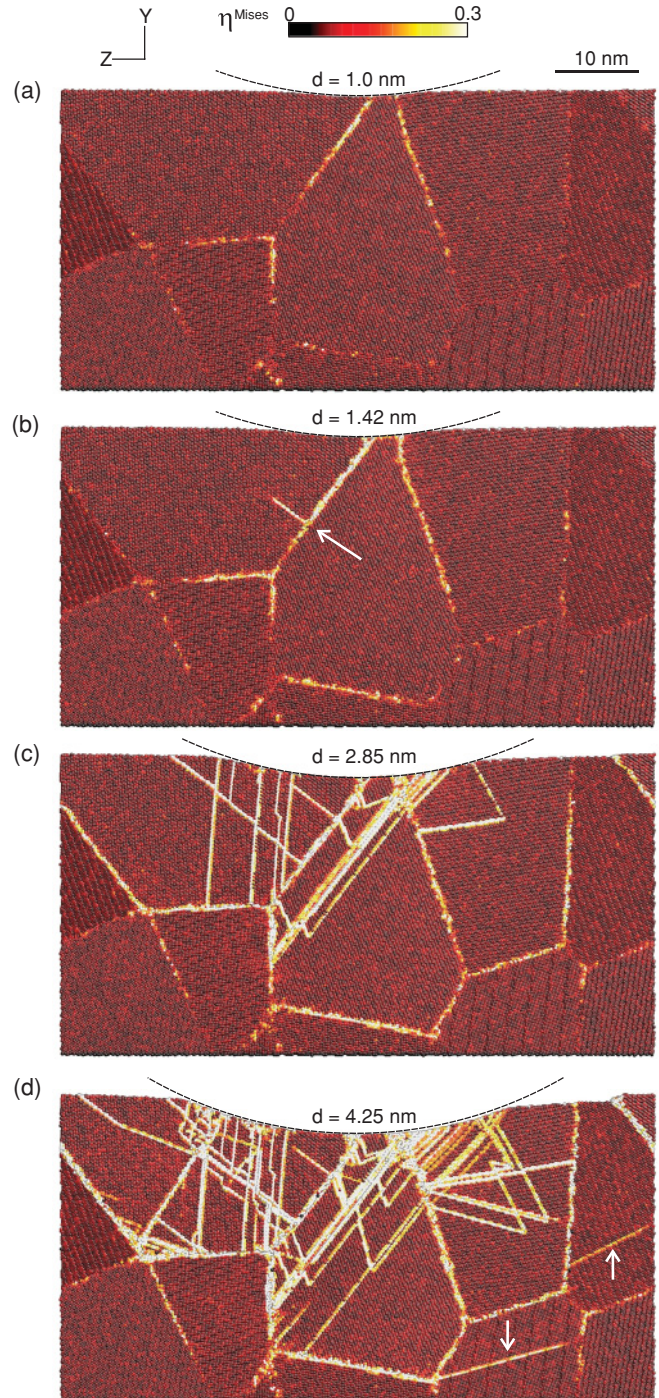


FIG. 6. (Color online) Calculations of the least-square atomic local shear-strain invariant η^{Mises} in the snapshots shown in Fig. 5. The figure shows that grain-boundary sliding already took place under the contact zone, before yielding by emission of lattice dislocations from grain boundaries.

nanostructures 1 and 2 is shown in Figs. 7 and 8, respectively. In both figures, the yield point is characterized by the nucleation and propagation of a partial dislocation from a grain boundary that is in direct contact with the tip. The local atomic shear-strain analysis provides clear evidence that grain-boundary sliding took place before the peak in nanohardness, as a function of penetration depth, was reached. In nanostructure 2

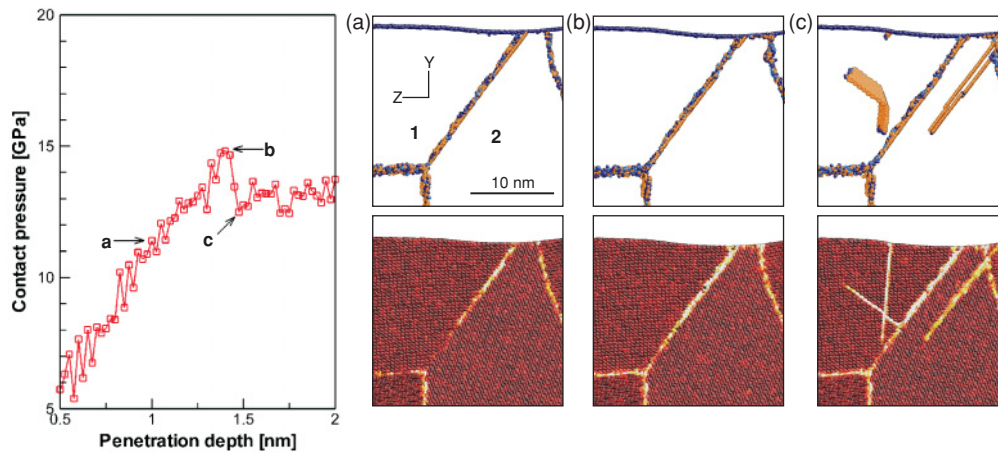


FIG. 7. (Color online) Dislocation processes near the contact zone during initial yielding of nanostructure 2 simulated by atomistic method.

(Fig. 7), sliding was observed to move gradually along the interface between grains 1 and 2. We can see in Fig. 7(c) that significant sliding was required to initiate the first dislocation-mediated yielding events. In nanostructure 1, sliding at all grain boundaries appeared more pronounced before the yield point [Figs. 8(a) and 8(b)]. However, it can be noticed that the interface orientation between grains 1 and 2 under the tip did not favor a high resolved shear stress for slip. This fact may explain why higher contact pressures were required in order to achieve yielding in this nanostructure, which further confirms that the primary yielding mechanism is due to crystal slip initiated from grain boundaries.

IV. DISCUSSION

The characterization of grain size and microhardness in the specimen investigated has confirmed that a fully dense Ni nanostructure with a critical grain size at the maximum of hardness has been successfully achieved in the present study. For the past 15 years, considerable attention has been paid to the mechanical properties of fcc metals in this grain-size regime. This interest is derived from the fact that the dependence of grain size on materials strength and hardness shows a reversed trend, as the grain size decreases, due to a fundamental change

in permanent deformation mechanisms from intragranular processes to intergranular processes.^{5,13,14,40,56,58} As such, metal nanostructures with the “strongest” size are expected to promote a peculiar behavior where both crystal slip mediated by grain boundaries and localized grain-boundary deformation such as sliding and migration can accommodate plastic flow under mechanical loading.

In the present study, two results point to the conclusion that the nanohardness of such nanostructures in electrodeposited Ni deformed by atomic-scale contact is controlled by a strong interplay between partial dislocation emission from grain boundaries and interface sliding. First, it should be emphasized that the initial microstructures simulated by MD in this work did not have impurities or point defects that could probably exist in electrodeposited materials. Particularly it is known that bath additives in Ni electrodeposits are preferentially deposited along grain boundaries. This effect is known to significantly increase the stress required to activate grain-boundary deformation and to reduce ductility in bulk nanostructures. However our study has shown good agreement between AFM experiments and MD simulations in terms of hardness measurements at this scale, despite significant sliding of the crystalline interfaces predicted for this grain size by MD simulations. This therefore suggests that plastic resistance

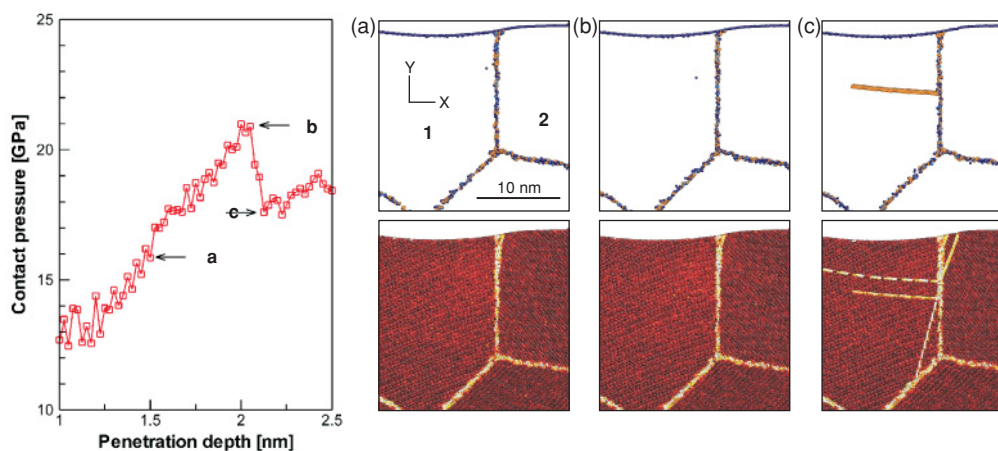


FIG. 8. (Color online) Dislocation processes near the contact zone during initial yielding of nanostructure 1 simulated by atomistic method.

and hardness are predominantly controlled by crystal slip initiated by the sliding of grain boundaries, as opposed to grain-boundary sliding only. Second, the experimental nanoindentation response has shown that the force–displacement curves present no discontinuity. Therefore it can be concluded that the onset of plasticity is not controlled by homogenous crystal slip. The present simulations have confirmed this hypothesis by showing that the process of partial dislocation emission from grain boundaries occurs in a continuing manner rather than intermittently, as the penetration depth increases. In addition, both predicted and measured nanohardness values did not significantly depend on the initial microstructure for contact depths larger than 2.5 nm, while the number of grains indented in the contact zone did not vary markedly for such shallow nanoindentations, as shown in Figs. 3(a), 3(c), and 3(d). This analysis therefore suggests that a large number of nucleation sites were located at crystalline interfaces away from the contact zone, as opposed to a homogenous crystal slip where yielding events are all localized at the tip–surface interface in coarse-grained materials.

The above dislocation process enables us to better interpret the nanoindentation size effect observed in nanocrystalline Ni films with very small grain sizes. In the past, Zong *et al.*⁶² have already reported the existence of nanoindentation size effects in single-crystalline Ni films under nanoindentation. They suggested that size effects at small penetration depths (<100 nm) result from source-limited deformation as the dislocation populations become sparser with decreasing depth. By analogy, we can hypothesize that nanoindentation size effects could also be observed in the present study because an increasing number of grain boundaries could emit new dislocations during the displacement of the tip, therefore resulting in a decreased hardness with increasing depth. This mechanism is also different from the nanoindentation size effect reported by Yang and Vehoff³⁷ in nanocrystalline Ni with larger grain sizes, which was related to the interaction of new dislocations with adjacent grain boundaries. We note, however, that the mean contact pressures predicted by our MD simulations showed no significant nanoindentation size effect for contact depths larger than 3.5 nm, i.e., for depths exceeding 10% of the film thickness, due to the influence of the rigid boundary in this type of simulations.

Furthermore, the good agreement between experiments and modeling shows that the tip velocity, which imposes the rate of deformation in the material, did not have any profound effect on the measured and predicted hardness values. This result is at odds with the facts that the tip velocity was several orders of magnitude larger in MD simulations (1 m s^{-1}) than in AFM experiments (1 nm s^{-1}), and that the hardness of bulk

Ni is known to promote increased strain-rate sensitivity with decreasing grain size.^{15,25,28} We think that this discrepancy relates to the confined scale at which our experiments and simulations were performed because strain-rate sensitivity effects in nanocrystalline fcc metals are mostly related to a state of generalized plasticity under large-scale deformation as opposed to incipient plastic flow behavior under confined contacts. Therefore this fundamental aspect is particularly relevant to the strain-rate sensitivity of plastic flow in nanoscale materials and devices under small contacts.

V. CONCLUSIONS

Electrochemical deposition of pure Ni on a polished Si(100) substrate was optimized in order to produce a flat nanocrystalline Ni substrate with the “strongest” size. A combination of AFM and large-scale MD simulation techniques with comparable scales of analysis in terms of grain size and contact zone size has been used to probe the nanoindentation behavior of this material at the atomic scale. This approach made it possible to characterize the mechanisms of permanent deformation under confined contact loading and to achieve accurate nanohardness measurements from shallow nanoindentations less than 10 nm in depth. We have demonstrated that the emission of partial dislocations from grain boundaries is the controlling yielding mechanism during nanoindentation in this model nanocrystalline metal. However, computer simulations have also revealed that significant grain-boundary sliding at small penetration depths precedes the initiation of crystal slip during nanoindentation. For penetration depths larger than 2.5 nm, however, both experiments and computer simulations point to a strong interplay between intragranular and intergranular deformation processes, which caused limited dependence of nanohardness on the microstructure initially indented. This phenomenon is contrary to observations made in the past in Ni films with larger grain diameters. These new findings provide better understanding of deformation and plastic resistance in nanocrystals under atomic-scale contact, which has significant implications in the synthesis of nanoscale materials and structures with improved mechanical resistance to contact loads.

ACKNOWLEDGMENT

We thank support from NSF CAREER program (Grant No. DMR-0747658), Vermont Experimental Program to Stimulate Competitive Research (Grant No. NSF EPS-0236976), and the computational resources of the Vermont Advanced Computing Center (Grant No. NASA NNX06AC88G).

*frederic.sansoz@uvm.edu

¹E. O. Hall, *Proc. Phys. Soc. London Sect. B* **64**, 747 (1951).

²N. J. Petch, *J. Iron Steel Inst.* **174**, 25 (1953).

³S. Yip, *Nature London* **391**, 532 (1998).

⁴A. S. Argon and S. Yip, *Philos. Mag. Lett.* **86**, 713 (2006).

⁵J. Schiotz, F. D. Di Tolla, and K. W. Jacobsen, *Nature (London)* **391**, 561 (1998).

⁶J. Schiotz, T. Vegge, F. D. Di Tolla, and K. W. Jacobsen, *Phys. Rev. B* **60**, 11971 (1999).

⁷H. Van Swygenhoven, M. Spaczer, A. Caro, and D. Farkas, *Phys. Rev. B* **60**, 22 (1999).

⁸H. Van Swygenhoven and P. M. Derlet, *Phys. Rev. B* **64**, 224105 (2001).

⁹A. Hasnaoui, H. Van Swygenhoven, and P. M. Derlet, *Phys. Rev. B* **66**, 184112 (2002).

- ¹⁰H. Van Swygenhoven, *Science* **296**, 66 (2002).
- ¹¹H. Van Swygenhoven, P. M. Derlet, and A. Hasnaoui, *Phys. Rev. B* **66**, 024101 (2002).
- ¹²P. M. Derlet, H. Van Swygenhoven, and A. Hasnaoui, *Philos. Mag.* **83**, 3569 (2003).
- ¹³K. S. Kumar, S. Suresh, M. F. Chisholm, J. A. Horton, and P. Wang, *Acta Mater.* **51**, 387 (2003).
- ¹⁴J. Schiötz and K. W. Jacobsen, *Science* **301**, 1357 (2003).
- ¹⁵R. Schwaiger, B. Moser, M. Dao, N. Chollacoop, and S. Suresh, *Acta Mater.* **51**, 5159 (2003).
- ¹⁶K. J. Van Vliet, S. Tsikata, and S. Suresh, *Appl. Phys. Lett.* **83**, 1441 (2003).
- ¹⁷Z. Budrovic, H. Van Swygenhoven, P. M. Derlet, S. Van Petegem, and B. Schmitt, *Science* **304**, 273 (2004).
- ¹⁸J. A. Knapp and D. M. Follstaedt, *J. Mater. Res.* **19**, 218 (2004).
- ¹⁹H. Van Swygenhoven, P. M. Derlet, and A. G. Froseth, *Nat. Mater.* **3**, 399 (2004).
- ²⁰V. Yamakov, D. Wolf, S. R. Phillpot, A. K. Mukherjee, and H. Gleiter, *Nat. Mater.* **3**, 43 (2004).
- ²¹E. M. Bringa, A. Caro, Y. M. Wang, M. Victoria, J. M. McNaney, B. A. Remington, R. F. Smith, B. R. Torralva, and H. Van Swygenhoven, *Science* **309**, 1838 (2005).
- ²²B. Zhu, R. J. Asaro, P. Krysl, and R. Bailey, *Acta Mater.* **53**, 4825 (2005).
- ²³F. Sansoz and V. Dupont, *Appl. Phys. Lett.* **89**, 111901 (2006).
- ²⁴H. Van Swygenhoven, P. M. Derlet, and A. G. Froseth, *Acta Mater.* **54**, 1975 (2006).
- ²⁵Y. M. Wang, A. V. Hamza, and E. Ma, *Acta Mater.* **54**, 2715 (2006).
- ²⁶D. H. Warner, F. Sansoz, and J. F. Molinari, *Int. J. Plasticity* **22**, 754 (2006).
- ²⁷F. A. Mohamed, *Metall. Mater. Trans. A* **38A**, 340 (2007).
- ²⁸H. Vehoff, D. Lemaire, K. Schuler, T. Waschkes, and B. Yang, *Int. J. Mater. Res.* **98**, 259 (2007).
- ²⁹V. Dupont and F. Sansoz, *Acta Mater.* **56**, 6013 (2008).
- ³⁰N. Q. Vo, R. S. Averback, P. Bellon, S. Odunuga, and A. Caro, *Phys. Rev. B* **77**, 134108 (2008).
- ³¹J. Li, K. J. Van Vliet, T. Zhu, S. Yip, and S. Suresh, *Nature (London)* **418**, 307 (2002).
- ³²K. J. Van Vliet, J. Li, T. Zhu, S. Yip, and S. Suresh, *Phys. Rev. B* **67**, 104105 (2003).
- ³³T. Zhu, J. Li, K. J. Van Vliet, S. Ogata, S. Yip, and S. Suresh, *J. Mech. Phys. Solids* **52**, 691 (2004).
- ³⁴J. Chen, W. Wang, L. H. Qian, and K. Lu, *Scrip. Mater.* **49**, 645 (2003).
- ³⁵D. Feichtinger, P. M. Derlet, and H. Van Swygenhoven, *Phys. Rev. B* **67**, 024113 (2003).
- ³⁶A. Hasnaoui, P. M. Derlet, and H. Van Swygenhoven, *Acta Mater.* **52**, 2251 (2004).
- ³⁷B. Yang and H. Vehoff, *Acta Mater.* **55**, 849 (2007).
- ³⁸E. T. Lilleodden, J. A. Zimmerman, S. M. Foiles, and W. D. Nix, *J. Mech. Phys. Solids* **51**, 901 (2003).
- ³⁹T. Tsuru, Y. Kaji, D. Matsunaka, and Y. Shibutani, *Phys. Rev. B* **82**, 024101 (2010).
- ⁴⁰J. R. Trelewicz and C. A. Schuh, *Acta Mater.* **55**, 5948 (2007).
- ⁴¹S.-Y. Chang and T.-K. Chang, *J. Appl. Phys.* **101**, 033507 (2007).
- ⁴²M. Chen, E. Ma, K. J. Hemker, H. Sheng, Y. Wang, and X. Cheng, *Science* **300**, 1275 (2003).
- ⁴³Y. T. Zhu, X. Z. Liao, and X. L. Wu, *Jom* **60**, 60 (2008).
- ⁴⁴M. Jin, A. M. Minor, E. A. Stach, and J. J. W. Morris, *Acta Mater.* **52**, 5381 (2004).
- ⁴⁵K. Zhang, J. R. Weertman, and J. A. Eastman, *Appl. Phys. Lett.* **87**, 061921 (2005).
- ⁴⁶S. Brandstetter, K. Zhang, A. Escudero, J. R. Weertman, and H. Van Swygenhoven, *Scrip. Mater.* **58**, 61 (2008).
- ⁴⁷F. Sansoz, K. D. Stevenson, R. Govinthasamy, and N. S. Murthy, *Scrip. Mater.* **59**, 103 (2008).
- ⁴⁸F. Sansoz and T. Gang, *Ultramicroscopy* **111**, 11 (2010).
- ⁴⁹S. Plimpton, *J. Comput. Phys.* **117**, 1 (1995).
- ⁵⁰Y. Mishin, D. Farkas, M. J. Mehl, and D. A. Papaconstantopoulos, *Phys. Rev. B* **59**, 3393 (1999).
- ⁵¹F. Sansoz and V. Dupont, *Scrip. Mater.* **63**, 1136 (2010).
- ⁵²V. Dupont and F. Sansoz, *J. Mater. Res.* **24**, 948 (2009).
- ⁵³G. J. Ackland and A. P. Jones, *Phys. Rev. B* **73**, 054104 (2006).
- ⁵⁴F. Shimizu, S. Ogata, and J. Li, *Mater. Trans.* **38**, 2923 (2007).
- ⁵⁵J. Li, *Mod. Simul. Mater. Sci Eng.* **11**, 173 (2003).
- ⁵⁶A. M. Elsharik and U. Erb, *J. Mater. Sci.* **30**, 5743 (1995).
- ⁵⁷F. Ebrahimi, G. R. Bourne, M. S. Kelly, and T. E. Matthews, *Nanostruct. Mater.* **11**, 343 (1999).
- ⁵⁸C. A. Schuh, T. G. Nieh, and T. Yamasaki, *Scrip. Mater.* **46**, 735 (2002).
- ⁵⁹R. Mishra and R. Balasubramaniam, *Corrosion Sci.* **46**, 3019 (2004).
- ⁶⁰Y. Li, H. Jiang, L. Pang, B. Wang, and X. Liang, *Surf. Coat. Technol.* **201**, 5925 (2007).
- ⁶¹K. L. Johnson, *Contact Mechanics* (Cambridge University Press, Cambridge, UK, 1987), p. 453.
- ⁶²Z. Zong, J. Lou, O. O. Adewoye, A. A. Elmustafa, F. Hammad, and W. O. Soboyejo, *Mater. Sci. Eng. A* **434**, 178 (2006).
- ⁶³F. Sansoz and J. F. Molinari, *Acta Mater.* **53**, 1931 (2005).